



Cite this: *Energy Environ. Sci.*, 2018, 11, 2993

# Elucidating lithium-ion and proton dynamics in anti-perovskite solid electrolytes†

James A. Dawson,<sup>a</sup> Tavleen S. Attari,<sup>b</sup> Hungru Chen,<sup>a</sup> Steffen P. Emge,<sup>c</sup> Karen E. Johnston<sup>b</sup> and M. Saiful Islam<sup>a</sup>

All-solid-state Li-ion batteries are currently attracting considerable research attention as they present a viable opportunity for increased energy density and safety when compared to conventional liquid electrolyte-based devices. The Li-rich anti-perovskite  $\text{Li}_{3-x}\text{OH}_x\text{Cl}$  has generated recent interest as a potential solid electrolyte material, but its lithium and proton transport capabilities as a function of composition are not fully characterised. In this work, we apply a combination of *ab initio* molecular dynamics and  $^1\text{H}$ ,  $^2\text{H}$  and  $^7\text{Li}$  solid-state NMR spectroscopy to study the mobility of lithium ions and protons in  $\text{Li}_{3-x}\text{OH}_x\text{Cl}$ . Our calculations predict a strongly exothermic hydration enthalpy for  $\text{Li}_3\text{OCl}$ , which explains the ease with which this material absorbs moisture and the difficulty in synthesising moisture-free samples. We show that the activation energy for Li-ion conduction increases with increasing proton content. The atomistic simulations indicate fast Li-ion diffusion but rule out the contribution of long-range proton diffusion. These findings are supported by variable-temperature solid-state NMR experiments, which indicate localised proton motion and long-range Li-ion mobility that are intimately connected. Our findings confirm that  $\text{Li}_{3-x}\text{OH}_x\text{Cl}$  is a promising solid electrolyte material for all-solid-state Li-ion batteries.

Received 15th March 2018,  
Accepted 30th July 2018

DOI: 10.1039/c8ee00779a

rsc.li/ees

## Broader context

Energy storage is a fundamental technology for a clean energy economy. However, substantial advancements in energy density compared to traditional Li-ion batteries are essential. One possible avenue to higher energy density, as well as improved operational safety, is the combination of a solid electrolyte with a lithium metal anode to create an all-solid-state battery. The discovery of new solid electrolytes and their optimisation are aided by the synergistic combination of computational chemistry and atomic-scale experimental characterisation. Here, we apply a combination of *ab initio* molecular dynamics and solid-state NMR spectroscopy to examine the mobility of lithium ions and protons in the promising anti-perovskite solid electrolyte material,  $\text{Li}_{3-x}\text{OH}_x\text{Cl}$ . We show that Li-ion transport is highly correlated with the proton and Li-ion vacancy concentrations, whilst confirming that proton hopping is restricted as a result of the large separation between oxygen ions. A new Li-ion hopping mechanism is proposed on the basis of the strong correlation between long-range Li-ion transport and  $\text{OH}^-$  rotation. Our results suggest that the Li-rich anti-perovskite system is an excellent candidate electrolyte for all-solid-state batteries.

## Introduction

Interest in fast Li-ion conducting solid electrolytes for the next generation of Li-ion batteries is ever increasing. By replacing the flammable liquid electrolytes currently used in commercial Li-ion batteries with solid electrolytes, the safety of the devices can be greatly enhanced.<sup>1–3</sup> In addition to the safety benefits,

solid electrolytes have the potential to enable the use of Li metal anodes, resulting in increased energy densities, and extended electrochemical windows.<sup>4–6</sup> A significant number of materials, typically based on the garnet, LISICON and perovskite structures, have been investigated as possible Li-ion solid electrolytes.<sup>7–11</sup>

Although the high Li-ion conductivities of Li-rich anti-perovskite materials have been known for decades,<sup>12,13</sup> it is only recently that significant interest has been generated for solid electrolyte applications.<sup>14–28</sup> Zhao and Daemen<sup>14</sup> reported high ionic conductivities ( $> 10^{-3} \text{ S cm}^{-1}$  at room temperature) and low activation energies (0.18–0.26 eV) for  $\text{Li}_3\text{OX}$ -based compositions, where X = Cl or Br. However, subsequent reports have noted reduced Li-ion conductivities and increased activation barriers for these materials.<sup>16–21,23</sup>

<sup>a</sup> Department of Chemistry, University of Bath, Bath, BA2 7AY, UK.

E-mail: j.a.dawson@bath.ac.uk, m.s.islam@bath.ac.uk

<sup>b</sup> Department of Chemistry, Durham University, Durham, DH1 3LE, UK.

E-mail: karen.johnston@durham.ac.uk

<sup>c</sup> Department of Chemistry, University of Cambridge, Cambridge, CB2 1EW, UK

† Electronic supplementary information (ESI) available. See DOI: 10.1039/c8ee00779a



It has been suggested that the as-prepared samples in the work of Zhao and Daemen were in fact hydrated compositions, *i.e.*,  $\text{Li}_2\text{OHCl}$ ,<sup>19</sup> based on their hygroscopic nature.<sup>12,13,15,19,22</sup> The measured ionic conductivities of these materials are known to be highly dependent on the sample preparation.<sup>16</sup>

Hood *et al.* explored  $\text{Li}_2\text{OHCl}$  as a potential solid electrolyte system and found that it possesses high Li-ion conductivity and a reasonable activation energy.<sup>15</sup> Li *et al.* reported that fluorine doping of  $\text{Li}_2\text{OHX}$  ( $\text{X} = \text{Cl}$  or  $\text{Br}$ ) resulted in a promising solid electrolyte with high Li-ion conductivity.<sup>19</sup> More recently, the ionic conductivities of  $\text{Li}_{3-x}\text{OH}_x\text{Cl}$  were measured as a function of proton concentration using impedance spectroscopy.<sup>22</sup>

However, the Li-ion and proton dynamics of the  $\text{Li}_{3-x}\text{OH}_x\text{Cl}$  system are not fully characterized, especially at the atomic scale. Here, *ab initio* molecular dynamics (AIMD) calculations and solid-state  $^1\text{H}$ ,  $^2\text{H}$  and  $^7\text{Li}$  NMR spectroscopy are used to study the dependence of Li-ion conductivity on the stoichiometry of the  $\text{Li}_{3-x}\text{OH}_x\text{Cl}$  system and to identify the contribution of proton transport. We show that the reaction of  $\text{Li}_3\text{OCl}$  and water is highly exothermic and that the activation energy for Li-ion transport increases with increasing proton concentration. Long-range proton transport is shown to be inhibited as a result of the large interatomic distances between adjacent oxygen ions.

## Methods

### *Ab initio* simulations

All calculations were performed using density functional theory (DFT) based on the Vienna *ab initio* simulation package (VASP).<sup>29</sup> A plane-wave cut-off energy of 400 eV, the projector augmented wave method<sup>30</sup> and the PBEsol exchange–correlation functional were employed. This functional has been used in previous successful studies of Li-ion battery materials.<sup>27,31–33</sup> The  $k$ -space was sampled with a  $k$ -point mesh spacing smaller than  $0.05 \text{ \AA}^{-1}$  and the gamma-point only for the reaction enthalpy and AIMD calculations, respectively. Structural optimisation was performed until the residual force on each atom was smaller than  $0.03 \text{ eV \AA}^{-1}$ . AIMD simulations were carried out to examine  $\text{Li}^+$  ion diffusion in  $\text{Li}_{3-x}\text{OH}_x\text{Cl}$  with  $4 \times 4 \times 4$  supercells containing 320 atoms. Each composition was first equilibrated for 10 ps. Statistical properties were then obtained from the following 50 ps simulations using the *NVT* ensemble with a Nose–Hoover thermostat.<sup>34</sup> The AIMD calculations were carried out at 600, 700, 800, 900 and 1000 K, with a short time step of 1 fs due to the presence of hydrogen. Self-diffusion data for Li were obtained from the mean square displacement (MSD) according to:

$$\langle r_i^2(t) \rangle = 6D_{\text{Li}}t \quad (1)$$

where  $\langle r_i^2(t) \rangle$  is the MSD,  $D_{\text{Li}}$  is the diffusion coefficient for Li and  $t$  is time. The diffusion coefficients were then converted to conductivities using the Nernst–Einstein relationship:

$$\frac{\sigma}{D_{\text{Li}}} = H_{\text{R}} \frac{nq^2}{kT} \quad (2)$$

where  $n$  is the number of charge carriers per unit volume,  $q$  is the electron charge,  $k$  is the Boltzmann constant,  $T$  is the temperature and  $H_{\text{R}}$  is the Haven ratio. A Haven ratio of one was used in our calculations. The methods described in this work have been successfully applied to examine Li-ion transport in a variety of solid electrolyte materials,<sup>35–37</sup> including  $\text{Li}_3\text{OX}$  ( $\text{X} = \text{Cl}$  or  $\text{Br}$ ),<sup>25,26,38</sup> and extend our previous computational work on Li-ion battery materials.<sup>39–44</sup>

### Synthesis and characterisation

Samples of  $\text{Li}_2\text{OHCl}$  were synthesised *via* solid-state methods. Stoichiometric amounts of commercial  $\text{LiCl}$  (Alfa Aesar, ultra dry, 99.9%) and  $\text{LiOH}$  (Acros Organics, anhydrous, 98%) were mixed and ground in an agate mortar and pestle inside an argon-filled glovebox. The powdered sample was placed in an alumina crucible and heated at  $350^\circ\text{C}$  for 30 min in a muffle furnace located inside the Ar-filled glovebox. Once the reaction was complete, the furnace was allowed to cool to room temperature and the sample was recovered. A sample of  $\text{Li}_2\text{OHCl}$  was deuterated for  $^2\text{H}$  NMR experiments using the same procedure outlined above, using the deuterated starting reagent  $\text{LiOD}$ .

Samples in the series  $\text{Li}_{3-x}\text{OH}_x\text{Cl}$ ,  $x = 0.25, 0.5$  and  $0.75$ , were also synthesised *via* a solid-state route using the same precursors. The powdered samples were placed in an alumina crucible that was placed inside a quartz tube. The quartz tube was sealed, removed from the glovebox, connected to a conventional Schlenk line apparatus and evacuated to  $10^{-3}$  mbar for 1 h. All samples were heated at  $350^\circ\text{C}$  for 30 min. Once the reaction was complete, the sealed quartz tube was removed from the furnace and allowed to cool to room temperature. Once cooled, the tube was returned to the Ar-filled glovebox, where the product was recovered. Post synthesis, the proton content of each sample was determined *via* integration of the appropriate  $^1\text{H}$  NMR spectrum, as detailed in the ESI.†

### X-ray diffraction

All samples were characterised by X-ray diffraction (XRD) using a Bruker d8 diffractometer using  $\text{Mo}$  ( $\lambda = 0.71073 \text{ \AA}$ ) radiation. Variable-temperature (VT) XRD patterns were obtained for  $\text{Li}_2\text{OHCl}$ , where the temperature was increased at a rate of  $2^\circ\text{C h}^{-1}$ .

### NMR spectroscopy

All solid-state NMR spectra were acquired using a Bruker 500 Avance III HD spectrometer, equipped with a wide-bore 11.7 T Oxford magnet, using Larmor frequencies of 499.69 MHz for  $^1\text{H}$  ( $I = 1/2$ ), 76.77 MHz for  $^2\text{H}$  ( $I = 1$ ) and 194.20 MHz for  $^7\text{Li}$  ( $I = 3/2$ ). Powdered samples were packed into conventional 4.0 mm  $\text{ZrO}_2$  rotors under an Ar atmosphere, and a magic-angle spinning (MAS) rate of 10 kHz was employed.  $^1\text{H}$  chemical shifts were referenced to neat tetramethylsilane, by setting the resonance from a sample of adamantane to  $\delta_{\text{iso}} = 1.9 \text{ ppm}$ .  $^7\text{Li}$  chemical shifts were referenced to 1 M  $\text{LiCl}_{(\text{aq})}$ .  $^2\text{H}$  chemical shifts were referenced to  $(\text{CD}_3)_4\text{Si}$  using a sample of  $\text{CDCl}_3$ ,  $\delta_{\text{iso}} = 7.24 \text{ ppm}$ .

Standard VT  $^1\text{H}$ ,  $^2\text{H}$  and  $^7\text{Li}$  MAS NMR experiments were completed for samples in the series  $\text{Li}_{3-x}\text{OH}_x\text{Cl}$



between  $-19$  and  $110$  °C using conventional hardware and the parameters detailed in the ESI.† Additional VT static  $^7\text{Li}$  NMR experiments were completed for  $\text{Li}_2\text{OHCl}$  over a temperature range of  $-65$  to  $230$  °C using a Bruker 400 Avance III HD spectrometer, equipped with a wide-bore 9.7 T magnet, using a Larmor frequency of 155.5 MHz for  $^7\text{Li}$ . The sample was packed into a 5.0 mm ceramic rotor inside an Ar-filled glove-box and placed into a Bruker 5.0 mm static probe. In all cases, quoted temperatures have been calibrated and reflect the true temperature of the sample during the experiment. Additional experimental details are given in the ESI.†

### Pulsed-field gradient (PFG)-NMR spectroscopy

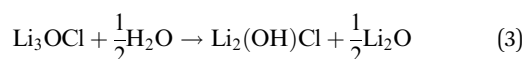
$^7\text{Li}$  PFG-NMR experiments were performed using a Bruker Diff50 PFG probe equipped with a Z-gradient and an EVT  $^7\text{Li}$  saddle coil in a 7.046 T magnet. Spectra were acquired using a stimulated diffusion pulse sequence (Scheme S1, ESI†) and varying gradient strengths. The effective gradient length,  $\delta$ , was set to 5 ms and a maximum gradient strength of  $1800\text{ G cm}^{-1}$  was used. The diffusion time,  $\Delta$ , was kept constant and set to either 100, 175 or 250 ms. Diffusion coefficients were obtained by fitting the decaying signal. All acquisitions were performed at an elevated temperature of 373 K. All samples were sealed into glass tubes under an Ar atmosphere.

## Results and discussion

### Hydration of $\text{Li}_3\text{OCl}$

The hygroscopic nature of the anti-perovskites has been shown experimentally.<sup>12,13,15,19</sup> In addition, it has been demonstrated that the preparation of  $\text{Li}_3\text{OX}$  ( $\text{X} = \text{Cl}$  or  $\text{Br}$ ) from dry  $\text{Li}_2\text{O}$  and  $\text{LiX}$  is challenging, even at high temperatures of 773–873 K.<sup>19</sup> This is in agreement with previous DFT calculations that predict  $\text{Li}_3\text{OX}$  to be metastable relative to  $\text{Li}_2\text{O}$  and  $\text{LiX}$ .<sup>45,46</sup>  $\text{Li}_3\text{OX}$  is usually prepared by annealing  $\text{LiOH}$  and  $\text{LiX}$  together.<sup>14,19</sup> The hydration of  $\text{Li}_3\text{OX}$  is charge-compensated by Li-ion vacancies.

To quantify the uptake of hydrogen in  $\text{Li}_3\text{OCl}$ , we first calculate its hydration enthalpy, based on the following reaction:



By computing the total energies of the reactants and products in reaction (3), we obtain a hydration enthalpy for the overall reaction of  $-0.74$  eV. Although there are no experimental values, this energy is consistent with measured calorimetry values for other perovskite oxides. Moreover, this strongly exothermic value confirms the favourable proton uptake of  $\text{Li}_3\text{OCl}$  and, hence, the difficulty in synthesising proton-free samples. This finding is in good agreement with our experimental observations, in which numerous synthetic procedures have been attempted to produce phase pure  $\text{Li}_3\text{OCl}$ , including varying the temperature and/or time of the reaction and altering the specific reaction environment. In each case, a complex mix of starting reagents and/or unknown phases is consistently produced, as shown by Fig. S1 (ESI†).

### Structures of $\text{Li}_{3-x}\text{OH}_x\text{Cl}$

Two phases have been confirmed for the hydrated phase,  $\text{Li}_2\text{OHCl}$ , using XRD.<sup>13</sup> Below  $\sim 308$  K,  $\text{Li}_2\text{OHCl}$  is reported to exist as an orthorhombic structure in space group  $\text{Amm}2$ . However, to date, no crystallographic information has been reported for this phase, although DFT-based techniques have been used in an attempt to rectify this.<sup>21</sup> Above this temperature,  $\text{Li}_2\text{OHCl}$  undergoes a phase transition to the cubic anti-perovskite phase with space group  $\text{Pm}\bar{3}\text{m}$ .<sup>13</sup> This phase transition, which is clearly observed during the present study *via* both VT XRD and  $^1\text{H}$  and  $^7\text{Li}$  MAS NMR studies (Fig. 1 and Fig. S2, ESI†), is known to increase the Li-ion conductivity by several orders of magnitude.<sup>13,15,19</sup> Moreover, it has been reported that the presence of cubic symmetry is a prerequisite for high ionic mobility in these materials.<sup>13</sup> There is a strong correlation between the Li motion and  $\text{OH}^-$  group rotation in  $\text{Li}_{3-x}\text{OH}_x\text{Cl}$ , with the  $\text{OH}^-$  groups being able to freely rotate in the cubic phase, whereas they are believed to be static in the orthorhombic phase as a result of the reduced Li motion (*vide infra*).<sup>13,47</sup>

In our calculations, we find that the ground state of  $\text{Li}_2\text{OHCl}$  is a tetragonal structure with all the  $\text{OH}^-$  groups aligned along the  $a$  direction. It is noteworthy that a tetragonal structure was also determined for  $\text{Li}_{2.17}\text{OH}_{0.83}\text{Cl}$  using XRD.<sup>13</sup> For the AIMD simulations, the cubic phase of  $\text{Li}_2\text{OHCl}$  was obtained by heating the tetragonal structure to high temperature. The  $\text{OH}^-$  groups are randomly orientated in the simulated cubic phase.

The tetragonal and cubic  $\text{Li}_2\text{OHCl}$  structures are illustrated in Fig. 2. In the conventional perovskite structure,  $\text{ABX}_3$ , the A and B sites are occupied by cations and the X site is an anion, whereas in the anti-perovskite structure, the A and B sites are occupied by anions and the X site is a cation. In  $\text{Li}_2\text{OHCl}$ , the B-site oxygen ion is coordinated to four  $\text{Li}^+$  ions and one proton, while the A-site  $\text{Cl}^-$  ion is coordinated to eight  $\text{Li}^+$  ions.

The calculated and experimental lattice parameters of the  $\text{Li}_{3-x}\text{OH}_x\text{Cl}$  compositions are given in Table 1, indicating good agreement. The results show that the lattice parameters remain mostly unaltered with increasing proton incorporation. This is also the case for the values obtained from XRD experiments. The contracted  $a$  lattice parameter of tetragonal  $\text{Li}_2\text{OHCl}$  is a result of the alignment of the  $\text{OH}^-$  groups along this direction, as shown in Fig. 2.

### Li-ion conductivity of $\text{Li}_{3-x}\text{OH}_x\text{Cl}$

It is possible to monitor ion mobility using variable temperature solid-state NMR spectroscopy. The  $^1\text{H}$  and  $^7\text{Li}$  MAS NMR spectra obtained for  $\text{Li}_2\text{OHCl}$  over the temperature range of  $-19$ – $106$  °C are shown in Fig. 1(b) and (c), respectively, where a single resonance is observed in each, indicating a single Li and H environment. In the VT  $^1\text{H}$  MAS NMR spectra (Fig. 1(b)), a narrowing of the lineshape is observed with increasing temperature. A corresponding plot of the full width at half maximum (FWHM) *vs.* temperature is shown in Fig. 1(d), which confirms a narrowing of the lineshape with increasing temperature. Between  $-19$  and  $33$  °C, there is minimal change in



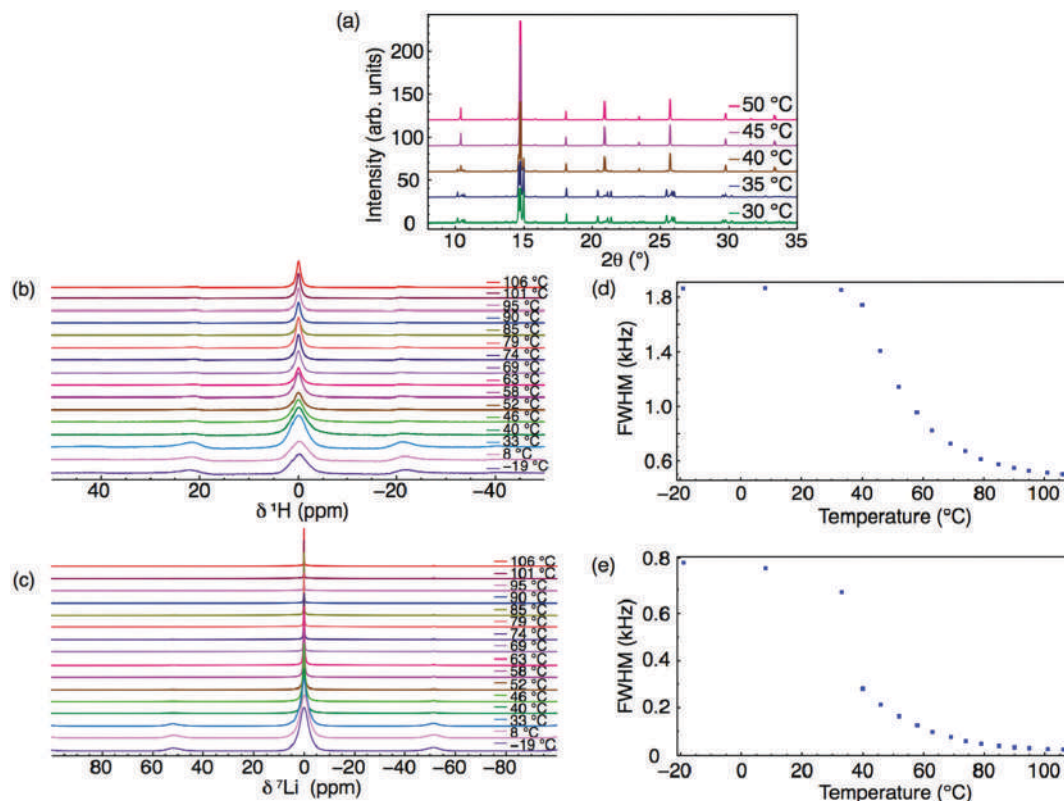


Fig. 1 VT (a) XRD patterns and (b) <sup>1</sup>H and (c) <sup>7</sup>Li MAS NMR spectra acquired for Li<sub>2</sub>OHCl between −19 and 106 °C. The corresponding variation in FWHM of <sup>1</sup>H and <sup>7</sup>Li are shown in (d) and (e), respectively. All spectra were acquired using a MAS rate of 10 kHz.

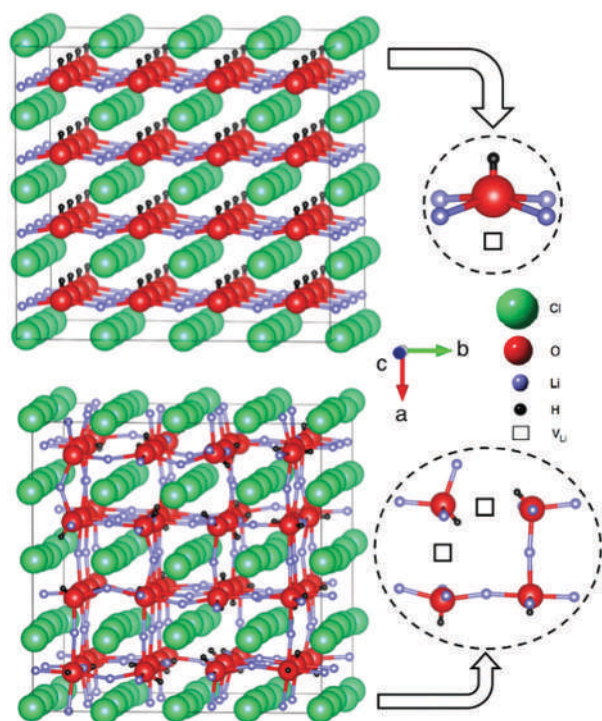


Fig. 2 Anti-perovskite structures of (a) tetragonal and (b) cubic Li<sub>2</sub>OHCl. The local coordination environments of the oxygen ions (to Li, H and Li vacancies, V<sub>Li</sub>) are also displayed.

Table 1 Lattice parameters of cubic Li<sub>3</sub>OCl, Li<sub>2.5</sub>OH<sub>0.5</sub>Cl and Li<sub>2</sub>OHCl, and tetragonal Li<sub>2</sub>OHCl

System	Calculation (Å)	Experiment (Å)
Li <sub>3</sub> OCl	<i>a</i> = 3.847	<i>a</i> = 3.907 <sup>48</sup>
Li <sub>2.5</sub> OH <sub>0.5</sub> Cl	<i>a</i> = 3.832	<i>a</i> = 3.909
Li <sub>2</sub> OHCl	<i>a</i> = 3.855	<i>a</i> = 3.913
Li <sub>2</sub> OHCl	<i>a</i> = 3.591, <i>b</i> = <i>c</i> = 3.853	—

the linewidth, suggesting the protons are static and not freely moving. As the temperature is increased to 52 °C, there is a sudden decrease in linewidth, believed to correspond to the known phase transition to the *Pm3m* phase. There is a further, more gradual, reduction in linewidth above 52 °C, believed to indicate the movement or mobility of protons within the structure, likely rotation or free movement of the OH<sup>−</sup> groups. However, it is noted that between 33 and 52 °C, it is challenging to accurately differentiate the precise contribution of the phase transition *versus* the mobility of the OH<sup>−</sup> groups to the change in linewidth.

Similar line narrowing is observed in the VT <sup>7</sup>Li NMR data (Fig. 1(c) and (e)). The phase transition from orthorhombic to cubic symmetry is clearly observed between 33 and 40 °C. Further line narrowing is observed as the temperature is increased, relating to mobile Li species within the structure. It is noted that the degree of line narrowing observed for <sup>7</sup>Li is





greater than that observed for  $^1\text{H}$ , suggesting Li has greater mobility in  $\text{Li}_2\text{OHCl}$  (*vide infra*).

Samples in the series  $\text{Li}_{3-x}\text{OH}_x\text{Cl}$  ( $x = 0.25, 0.5$  and  $0.75$ ) were synthesised and analysed *via* XRD and solid-state NMR spectroscopy. The XRD patterns obtained at room temperature for each composition are shown in Fig. 3(a), where the same phase observed for  $\text{Li}_2\text{OHCl}$  is also observed. The room temperature and VT  $^1\text{H}$  and  $^7\text{Li}$  MAS NMR spectra obtained for  $\text{Li}_{2.5}\text{OH}_{0.5}\text{Cl}$  are shown in Fig. 3(b) and (c), respectively. In each case, a single resonance is observed and, similar to  $\text{Li}_2\text{OHCl}$ , there is a reduction in the linewidth with increasing temperature, again suggesting both a phase change and ion mobility. The variation in FWHM with increasing temperature for  $^1\text{H}$  and  $^7\text{Li}$  is shown in Fig. 3(d) and (e). The changes observed are similar to those observed for  $\text{Li}_2\text{OHCl}$ , suggesting both protons and lithium ions are mobile at temperatures of  $>45^\circ\text{C}$ . Similar findings were observed for the remaining compositions in the series (see Fig. S3 and S4, ESI $^\dagger$ ). A comparison of the FWHM with changing composition is shown in Fig. S5 (ESI $^\dagger$ ). Small compositional changes appear to have little effect on the FWHM within this temperature range, as a similar reduction in linewidth is consistently observed across the series.

Fig. 4 shows representative mean square displacement plots for the  $\text{Li}_{3-x}\text{OH}_x\text{Cl}$  system at 800 K from the AIMD simulations. Several key points emerge from these plots. First, it is clear that with increasing proton concentration, there is a concomitant increase in Li-ion diffusion at this temperature. This is perhaps

unsurprising given the increase in Li vacancy concentration as a result of hydration. It is well known that Li vacancies are the dominant charge carriers in the anhydrous  $\text{Li}_3\text{OCl}$  material.<sup>27,28,38,45</sup> These results reinforce the fact that there is strong correlation between Li-ion transport and proton concentration.

Second, the increase in Li-ion diffusion extends beyond  $x = 1$ , *i.e.*,  $\text{Li}_2\text{OHCl}$ . This indicates that the formation of water molecules at low concentrations does not hinder Li-ion transport and the increasing Li vacancy concentration still dominates. However, for large proton concentrations ( $x = 2$ ), it is known experimentally that  $\text{LiOH}_2\text{Cl}$  (or  $\text{LiCl}\cdot\text{H}_2\text{O}$ ) is orthorhombic with space group  $\text{Cmcm}$ .<sup>13</sup> This is indicative of Li ordering, as confirmed by single crystal XRD studies,<sup>49</sup> and a reduction in Li-ion mobility. The poor Li-ion conductivity of  $\text{LiCl}\cdot\text{H}_2\text{O}$  was confirmed by Schwering *et al.*,<sup>13</sup> with the values dropping below the levels of detection ( $<10^{-8} \text{ S cm}^{-1}$ ) of the impedance analyser.

Third, in the  $\text{Li}_3\text{OCl}$  system ( $x = 0$ ), there is no Li diffusion due to the lack of Li vacancies. Disorder is usually introduced into this system *via*  $\text{LiCl}$  Schottky defect pairs, as found experimentally<sup>18</sup> and computationally.<sup>38</sup> Our calculations indicate that proton incorporation can provide an alternative mechanism for introducing disorder in the anti-perovskite material.

The self-diffusion coefficients for Li were converted into Li-ion conductivities and are presented as an Arrhenius plot

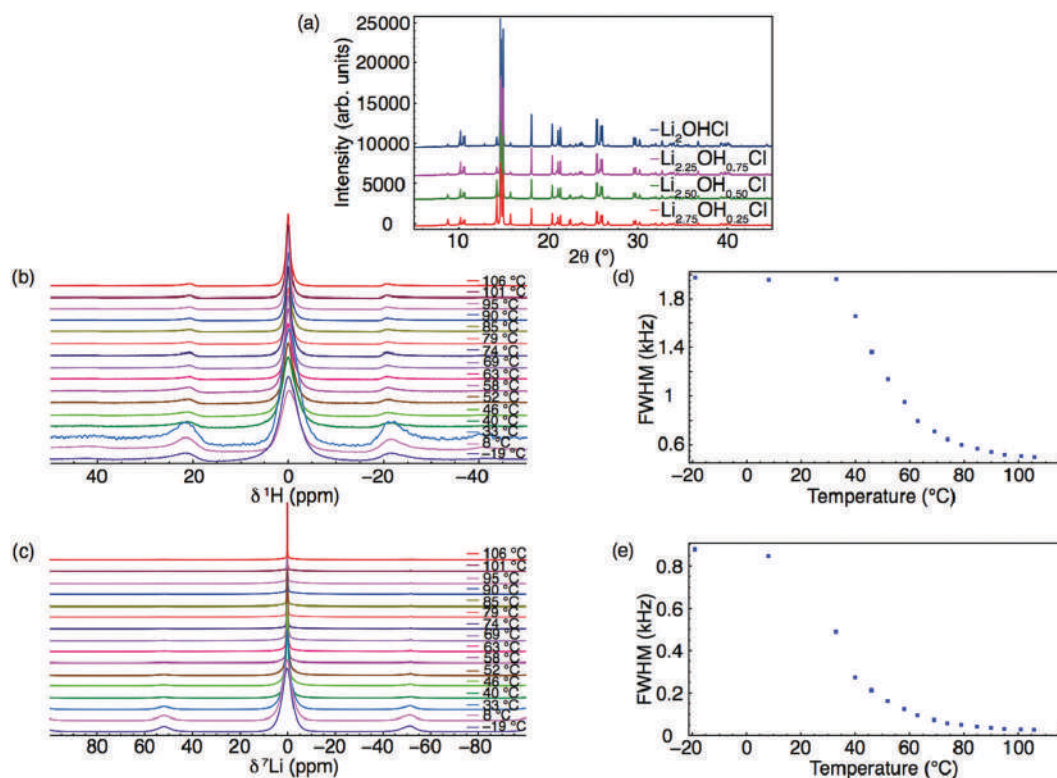


Fig. 3 (a) XRD patterns obtained for the series  $\text{Li}_{3-x}\text{OH}_x\text{Cl}$ , where  $x = 0.25, 0.5, 0.75$  and  $1$ . VT (b)  $^1\text{H}$  and (c)  $^7\text{Li}$  MAS NMR spectra obtained for  $\text{Li}_{2.5}\text{OH}_{0.5}\text{Cl}$ . The corresponding variation in FWHM of  $^1\text{H}$  and  $^7\text{Li}$  for  $\text{Li}_{2.5}\text{OH}_{0.5}\text{Cl}$  are shown in (d) and (e), respectively. All spectra were acquired using a MAS rate of 10 kHz.



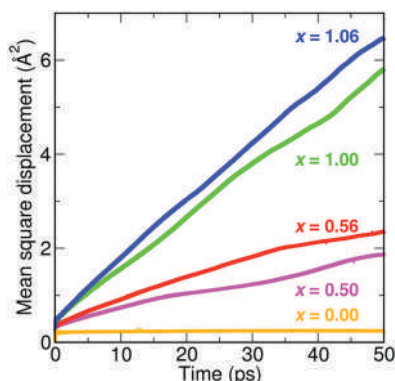


Fig. 4 MSD plots of  $\text{Li}^+$  in five different compositions of  $\text{Li}_{3-x}\text{OH}_x\text{Cl}$  at 800 K, showing higher Li-ion diffusion with increasing proton concentration.

in Fig. 5. The conductivity data of the four compositions can be divided into two groups. For low proton concentrations of  $x = 0.50$  and  $0.56$ , low activation barriers of  $0.32$  and  $0.30$  eV are obtained, respectively. For high proton concentrations of  $x = 1.00$  and  $1.06$ , slightly higher barriers of  $0.41$  and  $0.42$  eV, respectively, are found. It is clear that although the Li-ion conductivities of  $\text{Li}_2\text{OHCl}$  and  $\text{Li}_{1.94}\text{OH}_{1.06}\text{Cl}$  are higher than those of  $\text{Li}_{2.5}\text{OH}_{0.5}\text{Cl}$  and  $\text{Li}_{2.44}\text{OH}_{0.56}\text{Cl}$  at high temperatures ( $> 550$  K), they are significantly lower at typical solid-state battery operating temperatures ( $\sim 270$ – $400$  K). These results suggest that compositions with small proton concentrations ( $x \sim 0.5$ ) will have superior Li-ion transport properties in practical battery applications compared to compositions with high levels of protons.

We can compare our conductivity values to experiment by extrapolating our calculated values to lower temperatures. Hood *et al.*<sup>15</sup> obtained a conductivity of  $\sim 1 \times 10^{-4} \text{ S cm}^{-1}$  at  $373$  K for fast-cooled  $\text{Li}_2\text{OHCl}$ , which is in excellent agreement with our extrapolated value of  $\sim 1.7 \times 10^{-4} \text{ S cm}^{-1}$ . In addition,

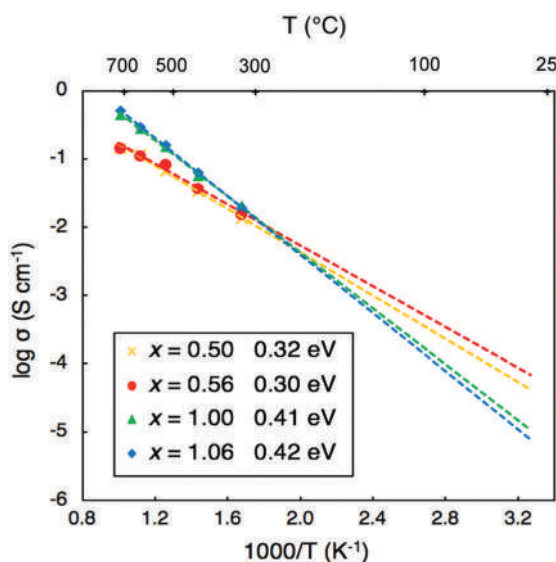


Fig. 5 Li-ion conductivities and activation energies of  $\text{Li}_{3-x}\text{OH}_x\text{Cl}$  derived from the AIMD simulations.

Li *et al.*<sup>19</sup> measured the Li-ion conductivity of  $\text{Li}_2(\text{OH})_{0.9}\text{F}_{0.1}\text{Cl}$ . They obtained a Li-ion conductivity of  $1.9 \times 10^{-3} \text{ S cm}^{-1}$  at  $373$  K, which is an order of magnitude higher than that measured for  $\text{Li}_2\text{OHCl}$ .<sup>15</sup> Fluorine doping was shown to both increase the Li-ion conductivity of  $\text{Li}_2\text{OHCl}$  and stabilise the cubic phase at room temperature.

Our calculated activation energy of  $0.41$  eV obtained for  $\text{Li}_2\text{OHCl}$  is comparable to the values of  $0.56$  and  $0.52$  eV determined by Hood *et al.*<sup>15</sup> and Li *et al.*,<sup>19</sup> respectively, using electrochemical impedance spectroscopy. It is interesting to note that the values of  $0.32$  eV for  $\text{Li}_{2.5}\text{OH}_{0.5}\text{Cl}$  and  $0.30$  eV for  $\text{Li}_{2.44}\text{OH}_{0.56}\text{Cl}$  are similar to the initial value of  $0.26$  eV for  $\text{Li}_3\text{OCl}$  determined by Zhao and Daemen.<sup>14</sup> More recently, Song *et al.*<sup>22</sup> reported low activation energies of  $0.24$ – $0.26$  eV for  $\text{Li}_{3-x}\text{OH}_x\text{Cl}$  ( $x = 0.3$ – $1.0$ ). The proposed reason for these low barriers was related to the ease with which these materials can form Schottky defects.

### Lithium-ion vs. proton transport

There has been debate over whether the Li-ion conductivities from impedance measurements may include contributions from fast proton transport in these materials.<sup>19</sup> To probe this issue, we plot the MSDs from our AIMD simulations for each element in  $\text{Li}_2\text{OHCl}$ , as shown in Fig. 6. While long-range diffusion for Li is clear from the linear increase of the MSD with time, this is not the case for proton transport as the proton MSD begins to flatten out before the end of the simulation time. In addition, the proton MSD never exceeds  $2 \text{ Å}^2$ , which is far below the O–O distance of  $3.91 \text{ Å}$  in  $\text{Li}_2\text{OHCl}$ .<sup>13</sup> This suggests that proton transport *via* the Grotthuss mechanism,<sup>50,51</sup> which is found in proton-conducting solid-oxide materials, does not occur in  $\text{Li}_2\text{OHCl}$ .

To gain further insight into proton and Li mobility within  $\text{Li}_2\text{OHCl}$ ,  $^1\text{H}$  and  $^7\text{Li}$   $T_1$  values were measured and are shown in Fig. 7. It is noted that to determine  $^7\text{Li}$   $T_1$  values, static  $^7\text{Li}$  NMR experiments were completed over a wider temperature window, namely,  $-65$  to  $230$  °C. The corresponding spectra are shown in Fig. 7(a). Below room temperature, the static  $^7\text{Li}$  NMR spectra exhibit the lineshape expected for a spin  $3/2$  nucleus, *i.e.*, a dipolar broadened lineshape at  $\sim 0$  ppm, corresponding to the central transition ( $+1/2 \leftrightarrow -1/2$ ). A broad resonance is also

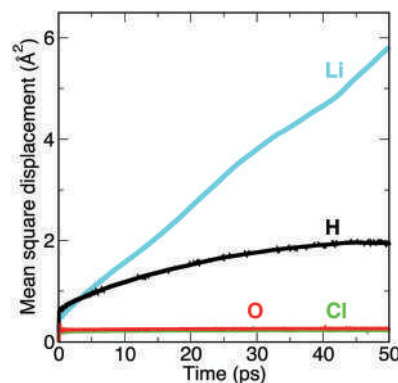


Fig. 6 MSD plots for each element in  $\text{Li}_2\text{OHCl}$  at  $800$  K.



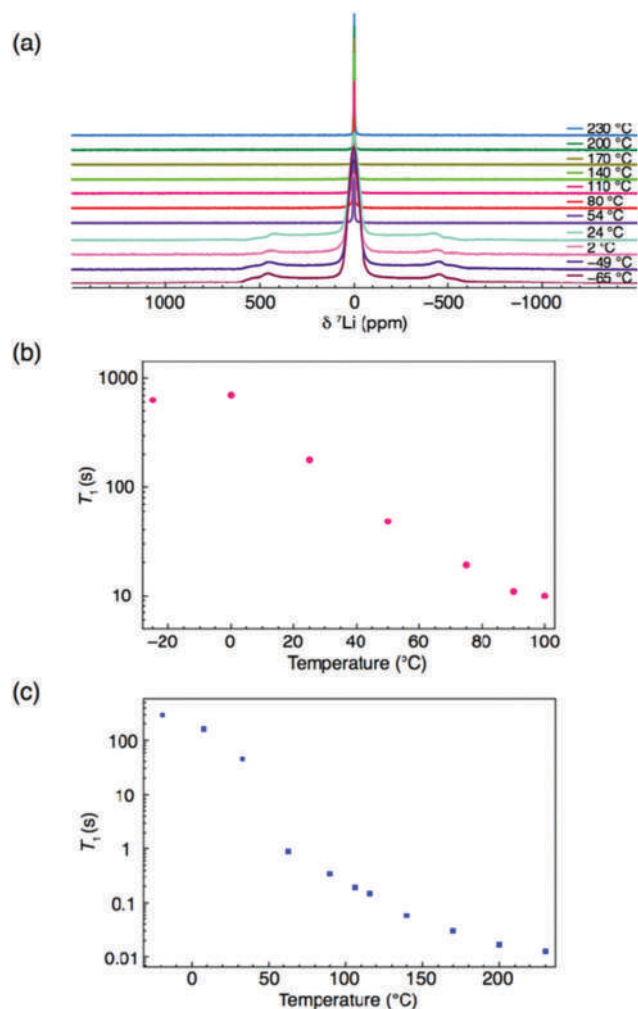


Fig. 7 NMR spectra for  $\text{Li}_2\text{OHCl}$ . (a) Static VT  $^7\text{Li}$  NMR spectra between  $-65$  and  $230$  °C. Also shown in (b) and (c) are the  $^1\text{H}$  and  $^7\text{Li}$   $T_1$  values.

observed, corresponding to the satellite transitions ( $3/2 \leftrightarrow 1/2$  and  $-1/2 \leftrightarrow -3/2$ ). Broadening of the central transition is due to strong  $^7\text{Li}$ - $^7\text{Li}$  homonuclear dipolar interactions that are averaged out as the temperature is increased. This is due to greater  $\text{Li}^+$  ion mobility and results in motional narrowing of the NMR linewidths.

All spectra obtained at temperatures  $> 54$  °C exhibit a single sharp resonance, corresponding to the cubic phase of  $\text{Li}_2\text{OHCl}$ . The corresponding FWHM plot vs. temperature is shown in Fig. S6 (ESI $^\dagger$ ), which confirms the phase transition occurring between 24 and 54 °C. Between 54 and 230 °C, there is a gradual reduction in the linewidth, indicative of Li ion mobility. The  $T_1$  values obtained (Fig. 7(b) and (c)) appear to indicate that Li is the more mobile species. In both cases, a rapid change in  $T_1$  is observed between 0 and  $\sim 60$  °C, believed to correspond to the expected phase change from orthorhombic to cubic symmetry. A more gradual change in  $^1\text{H}$   $T_1$  is then observed between 70 and 100 °C, where the value is on the order of seconds. This is in contrast to the  $^7\text{Li}$   $T_1$  measurements, where there is a gradual, but significant change between 90 and 230 °C, where

the value of  $T_1$  is 0.01 s. It is noted that only a limited temperature range could be studied for  $^1\text{H}$  based on current hardware limitations. However, comparing the  $^1\text{H}$  and  $^7\text{Li}$   $T_1$  values at 100 °C, there is an order of magnitude difference in the value of  $T_1$ . Such values of  $T_1$  suggest high Li mobility in  $\text{Li}_2\text{OHCl}$  and limited proton mobility.

Based on the current data it is likely that the protons are only locally mobile, *i.e.*, rotating or flipping around a localised point, whereas the Li can move freely throughout the structure. In good agreement with our *ab initio* simulations, these NMR results indicate that any conductivity within  $\text{Li}_2\text{OHCl}$  will be due to movement of the Li ions. Li-ion diffusion and limited proton mobility were further confirmed *via* PFG-NMR experiments, where the Li diffusion coefficient,  $D_{\text{Li}}$ , was determined to be  $\sim 6 \times 10^{-9} \text{ cm}^2 \text{ s}^{-1}$  at 373 K. Full details are given in the ESI $^\dagger$ . This value is in excellent agreement with our *ab initio* MD calculated value of  $\sim 3 \times 10^{-9} \text{ cm}^2 \text{ s}^{-1}$  extrapolated at 373 K.

To further investigate the local behaviour and mobility of the  $\text{OH}^-$  groups, a sample of  $\text{Li}_2\text{OHCl}$  was deuterated and studied using  $^2\text{H}$  solid-state NMR. Variable-temperature  $^2\text{H}$  MAS NMR data was acquired for  $\text{Li}_2\text{ODCl}$  at  $-19$ , 33, 63, 69, 95 and 110 °C (Fig. 8) and static  $^2\text{H}$  NMR data was acquired at  $-19$ , 69 and 110 °C (Fig. S12, ESI $^\dagger$ ). In both cases, between  $-19$  and 63 °C a classic, axially symmetric lineshape (MAS) and powder pattern (static) are obtained, indicative of the absence of motion and, hence, static  $\text{OH}^-/\text{OD}^-$  groups. The MAS lineshape was simulated and fitted (Fig. S13, ESI $^\dagger$ ) to obtain the quadrupolar NMR parameters,  $C_Q = 259(1) \text{ kHz}$  and  $\eta_Q = 0.0(1)$ , which are in good agreement with those commonly reported for static  $^2\text{H}$  environments.<sup>52</sup> The known phase transition from orthorhombic to cubic symmetry occurs at  $\sim 35$ – $40$  °C. The  $^2\text{H}$  NMR data presented indicates that even at 63 °C, when  $\text{Li}_2\text{ODCl}$  is known to be in the cubic phase, the  $\text{OH}^-/\text{OD}^-$  groups are still static, indicating that even though the phase transition has occurred, the  $\text{OH}^-/\text{OD}^-$  groups are not yet mobile. Hence, the phase transition *alone* is not responsible for mobility of the  $\text{OH}^-/\text{OD}^-$  groups.

At 69 °C, there is an obvious change in the appearance of the  $^2\text{H}$  MAS NMR spectrum (Fig. 8). The spectrum contains both a broad resonance and the axially symmetric lineshape previously observed at low temperatures. This suggests a change in the mobility of the  $\text{OH}^-/\text{OD}^-$  groups at this temperature and the presence of two different  $\text{OH}^-/\text{OD}^-$  environments simultaneously, *i.e.*, both static and mobile  $\text{OH}^-/\text{OD}^-$  groups. As the temperature is increased to 95 and 110 °C, a single, relatively broad resonance is observed, confirming mobility of the  $\text{OH}^-/\text{OD}^-$  groups.

It is well documented that for fast moving deuterons, a single, sharp “solution-like” lineshape (*e.g.*, 20 Hz), with very high intensity, will be observed in the  $^2\text{H}$  MAS NMR spectrum, owing to complete averaging of the quadrupolar tensor.<sup>53</sup> Such a sharp, narrow resonance is characteristic of a deuteron dissociating and being able to move freely throughout the structure.<sup>52,53</sup> Here, however, the linewidth of the resonance is still relatively large (*ca.* 2.7 kHz), suggesting movement of the  $\text{OD}^-$  group rather than that of a free deuteron, *i.e.*, rotation of





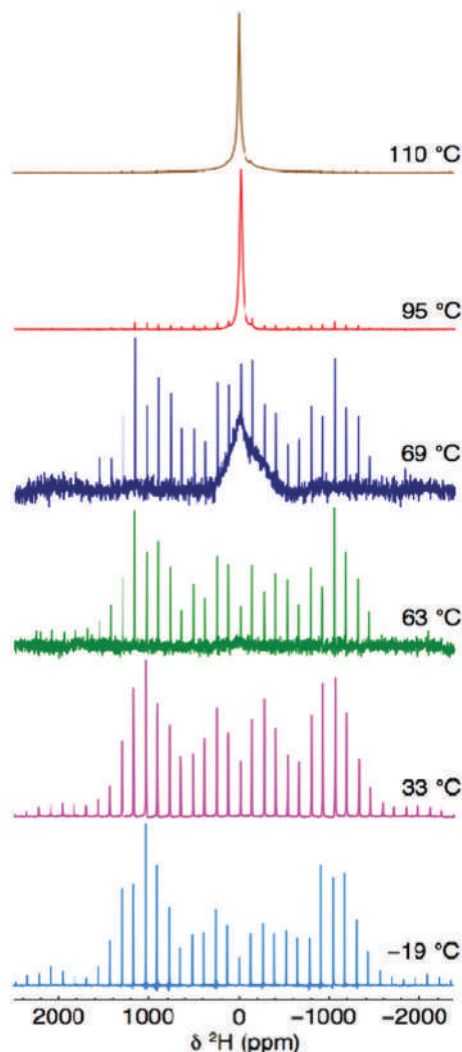


Fig. 8 Variable-temperature  $^2\text{H}$  MAS NMR spectra acquired for  $\text{Li}_2\text{ODCl}$  at  $-19$ ,  $33$ ,  $63$ ,  $69$ ,  $95$  and  $110$   $^\circ\text{C}$ . The MAS rate was  $10$  kHz.

the H/D around the oxygen (*vide infra*). It is also noted that at high temperatures ( $95$  and  $110$   $^\circ\text{C}$ ) the manifold of spinning sidebands remains (albeit at very low intensities), indicating the presence of static  $\text{OH}^-/\text{OD}^-$  groups. Hence, two different  $\text{OH}^-/\text{OD}^-$  environments are always present in the cubic phase of  $\text{Li}_2\text{ODCl}$ , both static and locally rotating  $\text{OH}^-/\text{OD}^-$  groups (*vide infra*).

Coupling these findings with our  $^1\text{H}$  and  $^7\text{Li}$  NMR data, we believe that mobility of the Li ions in  $\text{Li}_2\text{ODCl}$  is intimately connected to the position of the  $\text{OH}^-/\text{OD}^-$  groups within the structure. Based on both the experimental and computational data presented, we believe that the change from orthorhombic to cubic symmetry alone is not sufficient to increase the ionic conductivity of  $\text{Li}_2\text{OHCl}$ . Our AIMD calculations indicate that, in the cubic phase, the  $\text{OH}^-/\text{OD}^-$  groups point towards a Li vacancy and as the temperature is increased, the Li ions become mobile, starting to 'hop' into the Li vacancies and moving through the structure. As the temperature is increased further, the Li ions start to hop at a faster rate. Since the  $\text{OH}^-/\text{OD}^-$

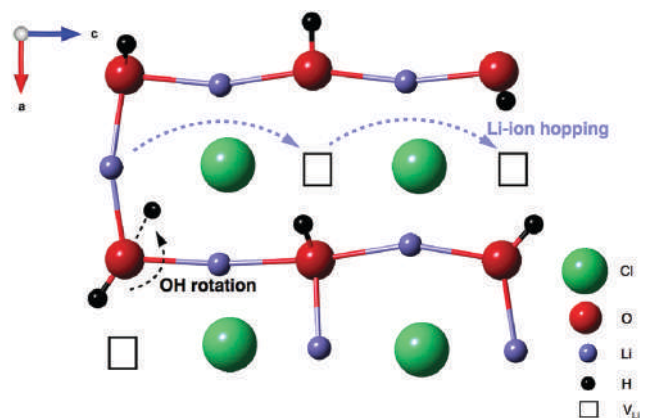


Fig. 9 Schematic representation of the Li-ion hopping mechanism in the cubic  $Pm\bar{3}m$  phase of  $\text{Li}_2\text{OHCl}$ . The  $\text{OH}^-$  groups point towards Li vacancies. Li-ion hopping occurs via these vacancies, denoted by the blue dashed arrows. Rotation of the  $\text{OH}^-$  groups occurs as a result of a nearby Li ion hopping to an adjacent site, denoted by the black dashed arrow.

groups point directly towards a Li vacancy, the movement of the Li ions will directly influence the position of the  $\text{OH}^-/\text{OD}^-$  groups, *i.e.*, when a Li vacancy is filled, the H/D will rotate around the oxygen, repositioning itself so that it is always pointing towards a vacancy, as it will therefore have the greatest degree of freedom and movement. Essentially, whatever the position of a Li vacancy, the  $\text{OH}^-/\text{OD}^-$  groups will reorient themselves to ensure they always point in the direction of a vacancy, as illustrated in Fig. 9.

Interestingly, in our AIMD calculations, there are O atoms coordinated to different numbers of Li ions, namely, three, four or five. For oxygen atoms coordinated to three Li ions, the proton movement is faster as it has more space to rotate into (because there are effectively three vacant sites). Conversely, for the O atoms coordinated to five Li ions, the movement is more restricted and hence the  $\text{OH}^-$  groups are limited in the spaces they can rotate into. Hence, the presence of multiple coordination environments in the supercell calculations correlates well with the  $^2\text{H}$  NMR findings, and the presence of both static and mobile  $\text{OH}^-/\text{OD}^-$  groups.

We also produce diffusion density maps from our AIMD simulations for Li and H in  $\text{Li}_2\text{OHCl}$ , given in Fig. 10, which are a sum of all the trajectories of these species accumulated over the length of the simulation. It can be seen for both Li and H that the largest densities are located around the corresponding crystallographic sites with considerable local oscillation. Moreover, significant Li-ion diffusion occurs via a vacancy mechanism, in which  $\text{Li}^+$  ions diffuse to adjacent vacant sites both diagonally and laterally to create long-range diffusion pathways. For  $\text{Li}_3\text{OCl}$ , we find significant Li-ion densities along the edges of the oxygen octahedra (shown in Fig. 10), which is indicative of the favourable migration pathways along these pathways, as found previously.<sup>28</sup>

In contrast, there are no long-range proton diffusion pathways, with only O–H rotational motion. This is perhaps unsurprising when we consider the O–O distance of  $3.91$  Å in these materials compared to proton-conducting perovskite





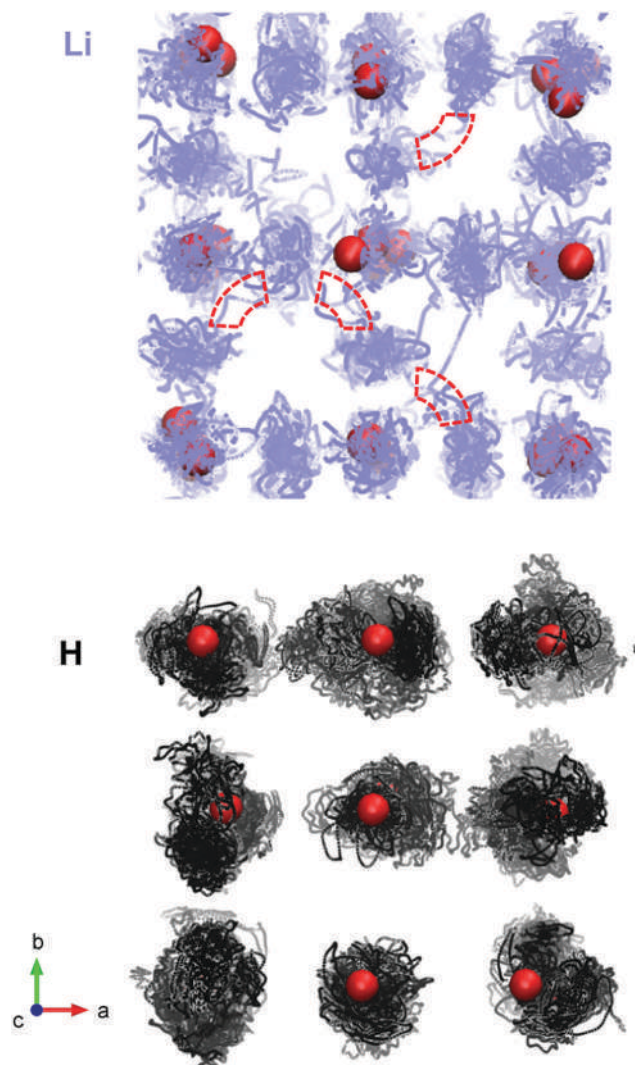


Fig. 10 Density plots of trajectories for lithium ions (blue) and protons (black) in  $\text{Li}_2\text{OHCl}$  at 800 K. Oxygen positions are given in red. Chlorine ions are omitted for clarity. Examples of local Li-ion jumps are highlighted with red dashed lines.

oxides, such as  $\text{BaZrO}_3$  (with an O–O separation of 2.97 Å).<sup>54</sup> Clearly, the large O–O distances in these anti-perovskite systems will inhibit significant proton hopping transport.

The important relationship between the Li-ion transport mechanism and O–H rotation in these systems has been recently reported by Song *et al.*<sup>22</sup> and Howard *et al.*<sup>21</sup> It was reported that short and fast rotating O–H bonds provide extra space that facilitates the formation of Frenkel defects, which are crucial in achieving fast, correlated Li-ion transport in these materials.<sup>22</sup>

Our simulation findings (Fig. 10) are in good agreement with the VT  $^1\text{H}$  and  $^7\text{Li}$  NMR data presented in Fig. 1, 7 and 8. As the temperature is increased, line narrowing is observed in both the  $^1\text{H}$  and  $^7\text{Li}$  NMR data. Hence, both the H and Li are, to some extent, mobile within the system. However, the changes observed in both the  $^1\text{H}$   $T_1$  values and the FWHM indicate that the protons are not as mobile as the Li. Higher  $^1\text{H}$   $T_1$  values and

reduced line narrowing indicate proton mobility is limited to rotation of the  $\text{OH}^-$  groups. This is further validated by the  $^2\text{H}$  MAS NMR data.

## Conclusions

Through an effective combination of *ab initio* molecular dynamics simulations and variable-temperature  $^1\text{H}$ ,  $^2\text{H}$  and  $^7\text{Li}$  MAS NMR spectroscopy, we have elucidated lithium-ion and proton transport mechanisms in the  $\text{Li}_{3-x}\text{OH}_x\text{Cl}$  solid electrolyte system. First, we report a high exothermic hydration enthalpy for  $\text{Li}_3\text{OCl}$ , which explains the ease with which this material absorbs moisture and the difficulty in synthesising moisture-free samples.

Second, we show that Li-ion transport is highly correlated with the proton concentration and Li-ion vacancy levels. Our calculations show long-range 3D diffusion of Li ions, but proton hopping is restricted as a result of the large separation between oxygen ions ( $\sim 4$  Å). There is excellent agreement between our calculated Li diffusion coefficient of the order  $10^{-9} \text{ cm}^2 \text{ s}^{-1}$  at 373 K and the value obtained from PFG-NMR measurements. Furthermore, proton incorporation can be used as a strategy for inducing disorder into the solid electrolyte systems and as a possible route to optimising the Li-ion conductivity.

Finally, these findings are supported by variable temperature  $^1\text{H}$ ,  $^2\text{H}$  and  $^7\text{Li}$  MAS NMR data, which indicate that proton movement is limited to rotation of the  $\text{OH}^-$  groups and that Li-ion mobility is long range. The presence of both static and locally mobile  $\text{OH}^-$  groups in the cubic phase of  $\text{Li}_2\text{OHCl}$  was confirmed using  $^2\text{H}$  NMR. Both the simulations and NMR experiments show that the protons point towards Li vacancy sites and that there is a strong correlation between long-range Li-ion transport and  $\text{OH}^-$  rotation.

Given the recent surge of interest in Li-rich anti-perovskite materials for solid electrolytes, atomic-scale studies of ionic conduction in the hydrated anti-perovskites are timely. The results presented here suggest that the  $\text{Li}_{3-x}\text{OH}_x\text{Cl}$  system is an excellent candidate electrolyte for all-solid-state batteries.

## Conflicts of interest

There are no conflicts to declare.

## Acknowledgements

We gratefully acknowledge support from the EPSRC Supergen Energy Storage Hub (EP/H019596), the EPSRC Programme Grant “Enabling next generation lithium batteries” (EP/M0009521/1), The Royal Society (RG170123) and the Archer HPC facility through the Materials Chemistry Consortium (EP/L000202/1). KEJ and TSA would also like to thank Dr David Apperley for experimental assistance.



## References

- 1 J. Janek and W. G. Zeier, *Nat. Energy*, 2016, **1**, 16141.
- 2 J. C. Bachman, S. Muy, A. Grimaud, H.-H. Chang, N. Pour, S. F. Lux, O. Paschos, F. Maglia, S. Lupart, P. Lamp, L. Giordano and Y. Shao-Horn, *Chem. Rev.*, 2016, **116**, 140–162.
- 3 A. Manthiram, X. Yu and S. Wang, *Nat. Rev. Mater.*, 2017, **2**, 16103.
- 4 D. Lin, Y. Liu and Y. Cui, *Nat. Nanotechnol.*, 2017, **12**, 194–206.
- 5 Y. Wang, W. D. Richards, S. P. Ong, L. J. Miara, J. C. Kim, Y. Mo and G. Ceder, *Nat. Mater.*, 2015, **14**, 1026–1031.
- 6 Y. Guo, H. Li and T. Zhai, *Adv. Mater.*, 2017, **29**, 1700007.
- 7 V. Thangadurai, H. Kaack and W. J. F. Weppner, *J. Am. Ceram. Soc.*, 2003, **86**, 437–440.
- 8 R. Murugan, V. Thangadurai and W. Weppner, *Angew. Chem., Int. Ed.*, 2007, **46**, 7778–7781.
- 9 P. G. Bruce and A. R. West, *J. Electrochem. Soc.*, 1983, **130**, 662–669.
- 10 R. Kanno, T. Hata, Y. Kawamoto and M. Irie, *Solid State Ionics*, 2000, **130**, 97–104.
- 11 S. Stramare, V. Thangadurai and W. Weppner, *Chem. Mater.*, 2003, **15**, 3974–3990.
- 12 P. Hartwig, A. Rabenau and W. Weppner, *J. Less-Common Met.*, 1981, **78**, 227–233.
- 13 G. Schwering, A. Hönnerscheid, L. van Wüllen and M. Jansen, *ChemPhysChem*, 2003, **4**, 343–348.
- 14 Y. Zhao and L. L. Daemen, *J. Am. Chem. Soc.*, 2012, **134**, 15042–15047.
- 15 Z. D. Hood, H. Wang, A. Samuthira Pandian, J. K. Keum and C. Liang, *J. Am. Chem. Soc.*, 2016, **138**, 1768–1771.
- 16 S. Li, J. Zhu, Y. Wang, J. W. Howard, X. Lü, Y. Li, R. S. Kumar, L. Wang, L. L. Daemen and Y. Zhao, *Solid State Ionics*, 2016, **284**, 14–19.
- 17 X. Lu, G. Wu, J. W. Howard, A. Chen, Y. Zhao, L. L. Daemen and Q. Jia, *Chem. Commun.*, 2014, **50**, 11520–11522.
- 18 X. Lü, J. W. Howard, A. Chen, J. Zhu, S. Li, G. Wu, P. Dowden, H. Xu, Y. Zhao and Q. Jia, *Adv. Sci.*, 2016, **3**, 1500359.
- 19 Y. Li, W. Zhou, S. Xin, S. Li, J. Zhu, X. Lü, Z. Cui, Q. Jia, J. Zhou, Y. Zhao and J. B. Goodenough, *Angew. Chem., Int. Ed.*, 2016, **55**, 9965–9968.
- 20 J. A. Dawson, P. Canepa, T. Famprikis, C. Masquelier and M. S. Islam, *J. Am. Chem. Soc.*, 2018, **140**, 362–368.
- 21 J. Howard, Z. D. Hood and N. A. W. Holzwarth, *Phys. Rev. Mater.*, 2017, **1**, 75406.
- 22 A.-Y. Song, Y. Xiao, K. Turcheniuk, P. Upadhyay, A. Ramanujapuram, J. Benson, A. Magasinski, M. Olguin, L. Meda, O. Borodin and G. Yushin, *Adv. Energy Mater.*, 2017, **8**, 1700971.
- 23 M. Wu, B. Xu, X. Lei, K. Huang and C. Ouyang, *J. Mater. Chem. A*, 2018, **6**, 1150–1160.
- 24 A. K. Sagotra, D. Errandonea and C. Cazorla, *Nat. Commun.*, 2017, **8**, 963.
- 25 A. K. Sagotra and C. Cazorla, *ACS Appl. Mater. Interfaces*, 2017, **9**, 38773–38783.
- 26 Z. Deng, B. Radhakrishnan and S. P. Ong, *Chem. Mater.*, 2015, **27**, 3749–3755.
- 27 S. Stegmaier, J. Voss, K. Reuter and A. C. Luntz, *Chem. Mater.*, 2017, **29**, 4330–4340.
- 28 R. Mouta, M. Á. B. Melo, E. M. Diniz and C. W. A. Paschoal, *Chem. Mater.*, 2014, **26**, 7137–7144.
- 29 G. Kresse and J. Furthmüller, *Phys. Rev. B: Condens. Matter Mater. Phys.*, 1996, **54**, 11169–11186.
- 30 J. P. Perdew, A. Ruzsinszky, G. I. Csonka, O. A. Vydrov, G. E. Scuseria, L. A. Constantin, X. Zhou and K. Burke, *Phys. Rev. Lett.*, 2008, **100**, 136406.
- 31 B. J. Morgan and P. A. Madden, *Phys. Rev. B: Condens. Matter Mater. Phys.*, 2012, **86**, 35147.
- 32 T. Baba and Y. Kawamura, *Front. Energy Res.*, 2016, **4**, 22.
- 33 J. A. Dawson, A. J. Naylor, C. Eames, M. Roberts, W. Zhang, H. J. Snaith, P. G. Bruce and M. S. Islam, *ACS Energy Lett.*, 2017, **2**, 1818–1824.
- 34 D. J. Evans and B. L. Holian, *J. Chem. Phys.*, 1985, **83**, 4069–4074.
- 35 L. J. Miara, S. P. Ong, Y. Mo, W. D. Richards, Y. Park, J.-M. Lee, H. S. Lee and G. Ceder, *Chem. Mater.*, 2013, **25**, 3048–3055.
- 36 R. Xiao, H. Li and L. Chen, *Sci. Rep.*, 2015, **5**, 14227.
- 37 C. Yu, S. Ganapathy, N. J. J. de Klerk, I. Roslon, E. R. H. van Eck, A. P. M. Kentgens and M. Wagemaker, *J. Am. Chem. Soc.*, 2016, **138**, 11192–11201.
- 38 Z. Lu, C. Chen, Z. M. Baiyee, X. Chen, C. Niu and F. Ciucci, *Phys. Chem. Chem. Phys.*, 2015, **17**, 32547–32555.
- 39 A. R. Armstrong, C. Lyness, P. M. Panchmatia, M. S. Islam and P. G. Bruce, *Nat. Mater.*, 2011, **10**, 223–229.
- 40 R. Tripathi, S. M. Wood, M. S. Islam and L. F. Nazar, *Energy Environ. Sci.*, 2013, **6**, 2257–2264.
- 41 D. A. Tompsett, S. C. Parker and M. S. Islam, *J. Am. Chem. Soc.*, 2014, **136**, 1418–1426.
- 42 Y. Deng, C. Eames, J.-N. Chotard, F. Lalère, V. Seznec, S. Emge, O. Pecher, C. P. Grey, C. Masquelier and M. S. Islam, *J. Am. Chem. Soc.*, 2015, **137**, 9136–9145.
- 43 J. A. Dawson and J. Robertson, *J. Phys. Chem. C*, 2016, **120**, 22910–22917.
- 44 P. Canepa, J. A. Dawson, G. Sai Gautam, J. M. Statham, S. C. Parker and M. S. Islam, *Chem. Mater.*, 2018, **30**, 3019–3027.
- 45 A. Emly, E. Kioupakis and A. Van der Ven, *Chem. Mater.*, 2013, **25**, 4663–4670.
- 46 M.-H. Chen, A. Emly and A. Van der Ven, *Phys. Rev. B: Condens. Matter Mater. Phys.*, 2015, **91**, 214306.
- 47 C. Eilbracht, W. Kockelmann, D. Hohlwein and H. Jacobs, *Phys. B*, 1997, **234**, 48–50.
- 48 O. Reckeweg, B. Blaschkowski and T. Schleid, *Z. Anorg. Allg. Chem.*, 2012, **638**, 2081–2086.
- 49 A. Hönnerscheid, J. Nuss, C. Mühle and M. Jansen, *Z. Anorg. Allg. Chem.*, 2003, **629**, 312–316.
- 50 N. Agmon, *Chem. Phys. Lett.*, 1995, **244**, 456.
- 51 P. Knauth and M. L. Di Vona, *Solid State Proton Conductors: Properties and Applications in Fuel Cells*, Wiley & Sons Ltd, 2012.
- 52 L. A. O'Dell and C. I. Ratcliffe, in *NMR of Quadrupolar Nuclei in Solid Materials*, ed. R. E. Wasylshen, S. E. Ashbrook and S. Wimperis, Wiley & Sons Ltd, Chichester, 2012, ch. 14, pp. 213–232.
- 53 G. Kim, F. Blanc, Y.-Y. Hu and C. P. Grey, *J. Phys. Chem. C*, 2013, **117**, 6504–6515.
- 54 J. A. Dawson, J. A. Miller and I. Tanaka, *Chem. Mater.*, 2015, **27**, 901–908.

